Earth and Planetary Science Letters 482 (2018) 454–469

Contents lists available at ScienceDirect

Earth and Planetary Science Letters

www.elsevier.com/locate/epsl

Quantifying Arabia–Eurasia convergence accommodated in the Greater Caucasus by paleomagnetic reconstruction

A. van der Boon [a,*], D.J.J. van Hinsbergen [a], M. Rezaeian [b], D. Gürer [a], M. Honarmand [b], D. Pastor-Galán [a,c], W. Krijgsman [a], C.G. Langereis [a]

[a] Utrecht University, The Netherlands
[b] Institute for Advanced Studies in Basic Sciences, Zanjan, Iran
[c] Center for Northeast Asian Studies, Tohoku University, Japan

ARTICLE INFO

Article history:
Received 23 June 2017
Received in revised form 20 September 2017
Accepted 9 November 2017
Available online xxxx
Editor: A. Yin

Keywords:
tectonic rotations
paleomagnetism
orocline
Eocene volcanics
Iran
Greater Caucasus

ABSTRACT

Since the late Eocene, convergence and subsequent collision between Arabia and Eurasia was accommodated both in the overriding Eurasian plate forming the Greater Caucasus orogen and the Iranian plateau, and by subduction and accretion of the Neotethys and Arabian margin forming the East Anatolian plateau and the Zagros. To quantify how much Arabia–Eurasia convergence was accommodated in the Greater Caucasus region, we here provide new paleomagnetic results from 97 volcanic sites (~500 samples) in the Talysh Mountains of NW Iran, that show ~15° net clockwise rotation relative to Eurasia since the Eocene. We apply a first-order kinematic restoration of the northward convex orocline that formed to the south of the Greater Caucasus, integrating our new data with previously published constraints on rotations of the Eastern Pontides and Lesser Caucasus. This suggests that north of the Talysh ~120 km of convergence must have been accommodated. North of the Eastern Pontides and Lesser Caucasus this is significantly more: 200–280 km. Our reconstruction independently confirms previous Caucasus convergence estimates. Moreover, we show for the first time a sharp contrast of convergence between the Lesser Caucasus and the Talysh. This implies that the ancient Paleozoic–Mesozoic transform plate boundary, preserved between the Iranian and East-Anatolian plateaus, was likely reactivated as a right-lateral transform fault since late Eocene time.

1. Introduction

Quantification of how convergence is accommodated in continental lithosphere in response to plate collisions – in this case the Arabia–Eurasia collision – is crucial for understanding the orogenic processes and related paleogeographic evolution such as the closure of marine gateways. However, there is often a deficit between estimates of crustal shortening and reconstructions of the amount of convergence from the plate circuit, as e.g. argued for in the India–Asia (Van Hinsbergen et al., 2012), or Iberia–Europe collision (Vissers et al., 2016). Such a mismatch between shortening and convergence has recently also been postulated for the Greater Caucasus on basis of seismological and sediment provenance data (Cowgill et al., 2016). Demonstrating such a mismatch, however, requires firm constraints on convergence, which is often controversial.

The Greater Caucasus mountain range, between the Black Sea and the Caspian Sea, is the world's second largest active orogen in a continental collision setting (Mumladze et al., 2015). Its relatively short length (~1100 km) and location within the overriding Eurasian part of the plate boundary zone, >350 km north of the suture with Arabia, make it an uncommon orogen. It is thought to have formed since the late Eocene (~35 Ma) through inversion of a Mesozoic back-arc basin during Arabia–Eurasia convergence and collision (e.g., Adamia et al., 2011a). The formation of the Greater Caucasus fold-thrust belt demonstrates that some of the 800–900 km of ~N–S Arabia–Eurasia convergence that occurred since 35 Ma along the strike of the Caucasus (McQuarrie and van Hinsbergen, 2013), was accommodated within the Eurasian part of the plate boundary zone. There is considerable debate on the timing of shortening and uplift of the Greater Caucasus Mountains, with estimates ranging from Eocene–Oligocene (Vincent et al., 2016) to Miocene (Forte et al., 2014). Forte et al. (2014) recognized that the Greater Caucasus is made up of several distinct structural zones which may reflect lateral differ-

* Corresponding author.
E-mail address: avanderboon.work@gmail.com (A. van der Boon).

https://doi.org/10.1016/j.epsl.2017.11.025
0012-821X/

ences in amount of accommodated shortening and convergence along the mountain range. In any case, the geological and seismological estimate of Greater Caucasus shortening and subduction may have been 130 to as much as 400 km (Cowgill et al., 2016; Ershov et al., 2003). The remainder of Arabia–Eurasia convergence then has to be accommodated by subduction within or below the East Anatolian and Iranian plateaus.

Constraining how this convergence was partitioned is particularly complex due to the general absence of detailed structural geologic constraints on Caucasus shortening. Moreover, geologically recorded shortening may underestimate the total amount of convergence if wholesale lithospheric subduction occurred without accretion. Paleomagnetic inclinations may be used to determine paleolatitudinal convergence if convergence is larger than paleomagnetic error bars of typically some 5° (∼500 km), which is unlikely in the Caucasus case. Cowgill et al. (2016) recently suggested that higher convergence in the Greater Caucasus than in the neighboring Black Sea and Caspian Sea regions led to the formation of the Pontide–Lesser Caucasus–Talysh orocline, which extends from the eastern Pontides (NE Turkey), through the Lesser Caucasus (e.g. Bazhenov and Burtman, 2002 and Meijers et al., 2015 and references therein). Here, we therefore explore a novel quantitative geometrical constraint on the amount of Arabia–Eurasia convergence that was accommodated in the Greater Caucasus region since the late Eocene by paleomagnetically restoring the vertical axis rotations accommodated during the formation of this orocline, which we extend towards the Talysh Mountains of Iran (Fig. 1). We use paleomagnetic estimates of net post-Eocene rotation from the limbs of this orocline to restore the convergence accommodated in the Greater Caucasus. Large datasets are available from the western limb in Turkey (Hisarlı, 2011), as well as from the central, Lesser Caucasus segment (Meijers et al., 2015). In the western part of the Alborz mountains, data were collected by Cifelli et al. (2015). We here provide new paleomagnetic constraints on the amount of rotation of the eastern limb of the orocline, in the Talysh Mountains of Iran. Then, we develop a first-order kinematic restoration of the orocline to constrain the minimum amount of northward motion of the Lesser Caucasus relative to the Black Sea and Caspian Sea regions since the Eocene. We use this reconstruction to quantify how convergence was partitioned over the Caucasus orogen and plateaus to the south.

2. Geological setting

2.1. Regional geology

The Caucasus orogen is located along the southern fringes of the Scythian platform of Eurasia. To the south are a series of accreted Gondwana-derived continental blocks that collided with Eurasia upon closure of the Paleotethys and Neotethys oceans in Paleozoic to Cenozoic times (e.g. Barrier et al., 2008). In Iran, Gondwana-derived 'Cimmerian' blocks collided with Eurasia in the Late Triassic, closing the Paleotethys ocean after which they were shortened in the Neogene during Arabia–Eurasia collision by up to ∼175 km (McQuarrie and van Hinsbergen, 2013; Mouthereau et al., 2012). NW Iran consists of at least two Cimmerian blocks, the Sanandaj-Sirjan block and the Alborz block. Neotethys subduction below the Iranian Cimmerian blocks occurred from the Jurassic until the final collision of Arabia with Eurasia (Agard et al., 2011). Present shortening estimates of the Iranian plateau and the Zagros mountains suggest that collision must have been underway by 20 Ma, and may have started around 27–28 Ma (McQuarrie and van Hinsbergen, 2013 and references therein). In Turkey, the tectonic history is different. In the west, at least two Gondwana-derived continental fragments collided with Eurasia (Pontides and Anatolide-Taurides), while in eastern Turkey a long-lived, oceanic crust-derived accretionary prism formed that underlies most of the east Anatolian plateau. The Turkish and Iranian systems were separated by a plate boundary since the Permian (Stampfli and Borel, 2002), probably in the form of a major transform fault system. Eastern Mediterranean paleogeographic reconstructions suggest that this transform may have been reactivated since the early Eocene (visualized in Barrier et al., 2008). The Arax valley fault, on the border between Armenia, Iran and Azerbaijan (Jackson and Mckenzie, 1983) may be a remnant of this ancient plate boundary (Fig. 1).

The Lesser Caucasus region is located to the south of the Greater Caucasus, and is formed by volcanic arc material of Jurassic to Eocene age, which connects to the Pontides in the west and the Talysh in the east during Eocene volcanism (e.g. Adamia et al., 2011b). This region is bordered from the Gondwana-derived South Armenian block to the south by the ophiolitic Sevan-Akera suture (e.g. Rolland et al., 2012; Sosson et al., 2010).

As there are no tectonic maps of the entire studied region, we compiled a new tectonic map (Fig. 1) from the maps of Adamia et al. (2011b); Şengör et al. (2003); Zanchetta et al. (2009), and we added faults from Dilek and Altunkaynak (2010) and Solaymani Azad et al. (2011). All maps were georeferenced, overlain on top of each other and subsequently checked using a digital elevation model in discerning tectonic regions.

2.2. Geology of the Talysh

The geology of the Talysh and Alborz consists of Precambrian up to Quaternary rocks, with abundant Eocene volcanic rocks. The Precambrian and Cambrian make up around 3.5 km and consist mostly of sandstone and dolomite. Silurian and Ordovician units consist of limestone and some basic volcanic rocks. The Devonian is characterized by deposition of limestone, with an unconformity separating it from the underlying Silurian. Post-Silurian basic volcanic rocks are covered by Permo-Carboniferous limestone and lower Carboniferous andesite. The Talysh contains remnants of an Upper Paleozoic ophiolite belt, which is related to closure of a Hercynian ocean. The Triassic–Jurassic consists of shales, sandstones and conglomerates, and is around 4 km thick. During the Upper Jurassic and Cretaceous, shallow marine limestones were deposited in the Talysh and Alborz, which make up around 600 meters (Berberian and King, 1981; Zanchi et al., 2006). Some Cretaceous volcanic rocks with a within-plate signature are also present in the Central Alborz (Doroozi et al., 2016). The Paleogene in the Alborz consists of the Fajan formation, comprising up to 200 meters of continental conglomerates. This formation is covered by Paleocene–middle Eocene nummulitic limestones of the Ziarat formation (100–300 m thick). The top of this formation is of Lutetian age (middle Eocene) in the Alborz, while further east, in the Kopeh Dagh, it extends into the Priabonian (late Eocene) (Gravand and Golgir, 2014). After the Lutetian, a flare-up of volcanism led to deposition of the Karaj formation, which is up to 9 km thick (Verdel et al., 2011), and has a continental arc geochemical signature (van der Boon et al., 2015). During the Oligocene, compression in the region led to uplift and erosion, causing deposition of coarse-grained clastic sedimentary rocks (Morley et al., 2009; Vincent et al., 2005).

There are many large faults present in the region, although these are relatively unstudied. Both thrust faults and strike-slip faults are present in the region, with strike-slip faults showing left lateral motion (e.g. Jackson et al., 2002). The faults in the Alborz and the Talysh are different from each other, with faults in the Talysh having nearly flat fault planes on which thrusting occurs. The motion along faults is disputed. For example, Jackson et al. (2002) interpret the Astara fault as a thrust (Fig. 2), while on 1:100.000 series geologic maps (Geologic Survey of Iran), it is

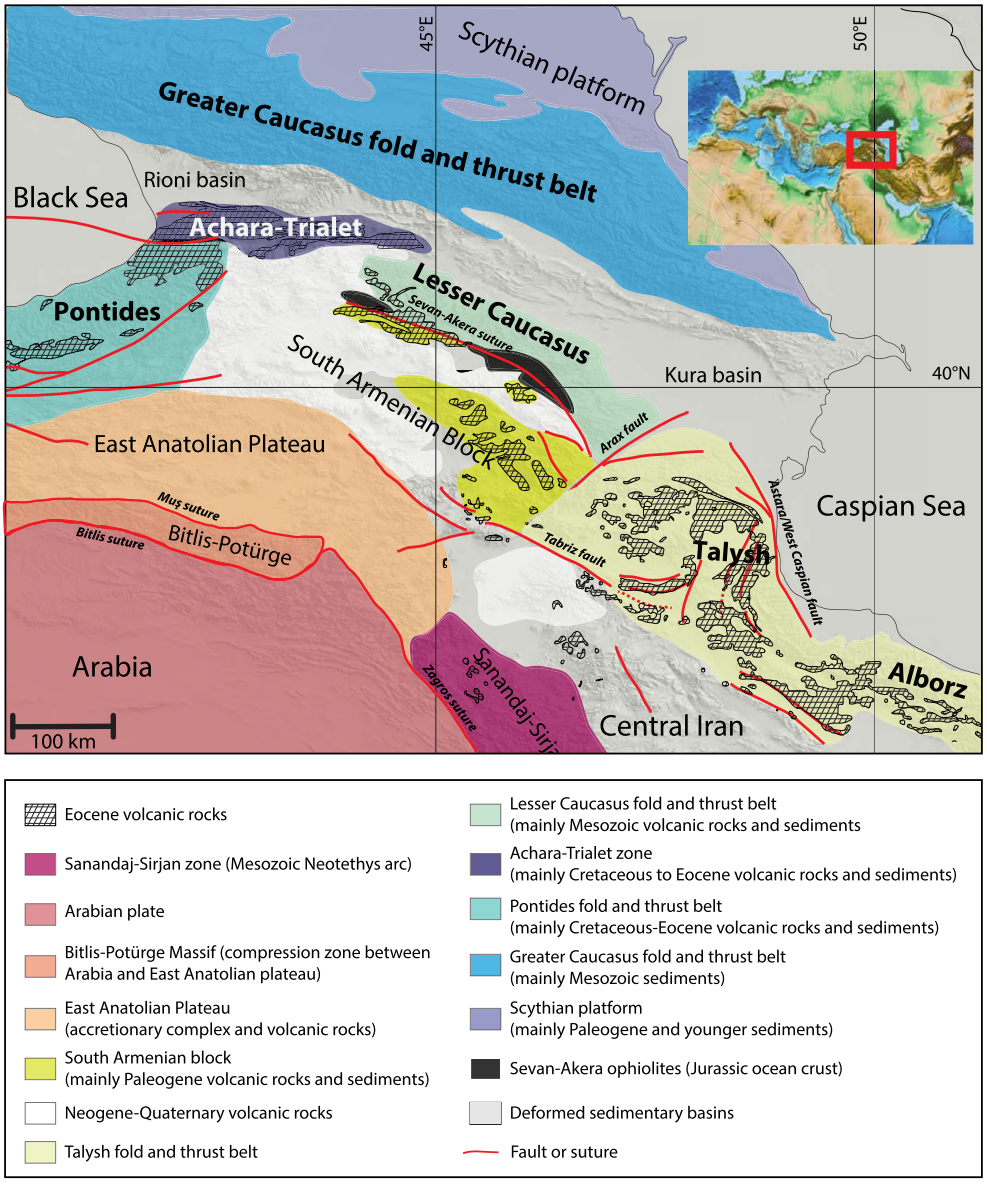

Fig. 1. Simplified geological map of the Caucasus, Talysh and Alborz region and the main tectonic units (modified after: Adamia et al., 2011b; Şengör et al., 2003; Zanchetta et al., 2009). Faults are after Dilek and Altunkaynak, 2010; Solaymani Azad et al., 2011.

drawn as a strike-slip fault. Faults as shown in Fig. 2 are compiled from 1:100.000 series geologic maps (Geologic Survey of Iran), and the studies of Jackson et al. (2002) and Rezaeian et al. (2012), with the nature of the faults drawn tentatively.

3. Methods

Sampling was carried out in 2014, along the belt of Eocene volcanics which forms the Talysh mountain range in NW Iran, from the border with Azerbaijan in the north, to the south-east until Kakajin. In total, 97 sites of Eocene rocks were sampled which we logically grouped into 11 localities (Fig. 2). By far the majority of rocks were lava flows and volcaniclastic rocks, ranging in composition from basaltic lavas and andesites to tuff breccias and ignimbrites. From the 97 sites, only 9 sites were taken in sedimentary rocks, mostly fine-grained volcaniclastic and tuffaceous sedimentary rocks; the remaining 88 sites were drilled in lava flows, where each single flow is designated one site. Lava flows typically record spot readings of the magnetic field and tend to give concentrated (low dispersion, high k value) directional distributions, with a dispersion parameter k often higher than 100. In this study, we follow the slightly more lenient criterion of $k > 50$ (Biggin et al., 2008). Common paleomagnetic statistics typically require 5–7 samples per lava flow to give a good estimate of k. However, due to the extremely hard lithology of the volcanic rocks in most sites and the long time it took to drill a single core (up to 15 min), we compromised by taking less samples per flow (minimum of 3) but sampling more lava flows per locality. More than 500 standard paleomagnetic samples (25 mm diameter cores) were drilled using a gasoline-powered drill; the cores were cut in the laboratory into standard (22 mm) specimens. Samples with a high intensity natural remanent magnetization and exceeding the dynamic range of the cryogenic magnetometer were subsequently cut in half.

The specimens were subjected to thermal and/or alternating field (AF) demagnetization. Temperature increments of 20–80 °C were applied to thermally demagnetize the samples in a shielded ASC TD48-SC oven, up to a maximum temperature of 680 °C. Demagnetization steps ranging 5–100 mT with field steps of 5 or 10 mT were applied for AF demagnetization. The magnetization after each step was measured on a 2G Enterprise horizontal cryo-

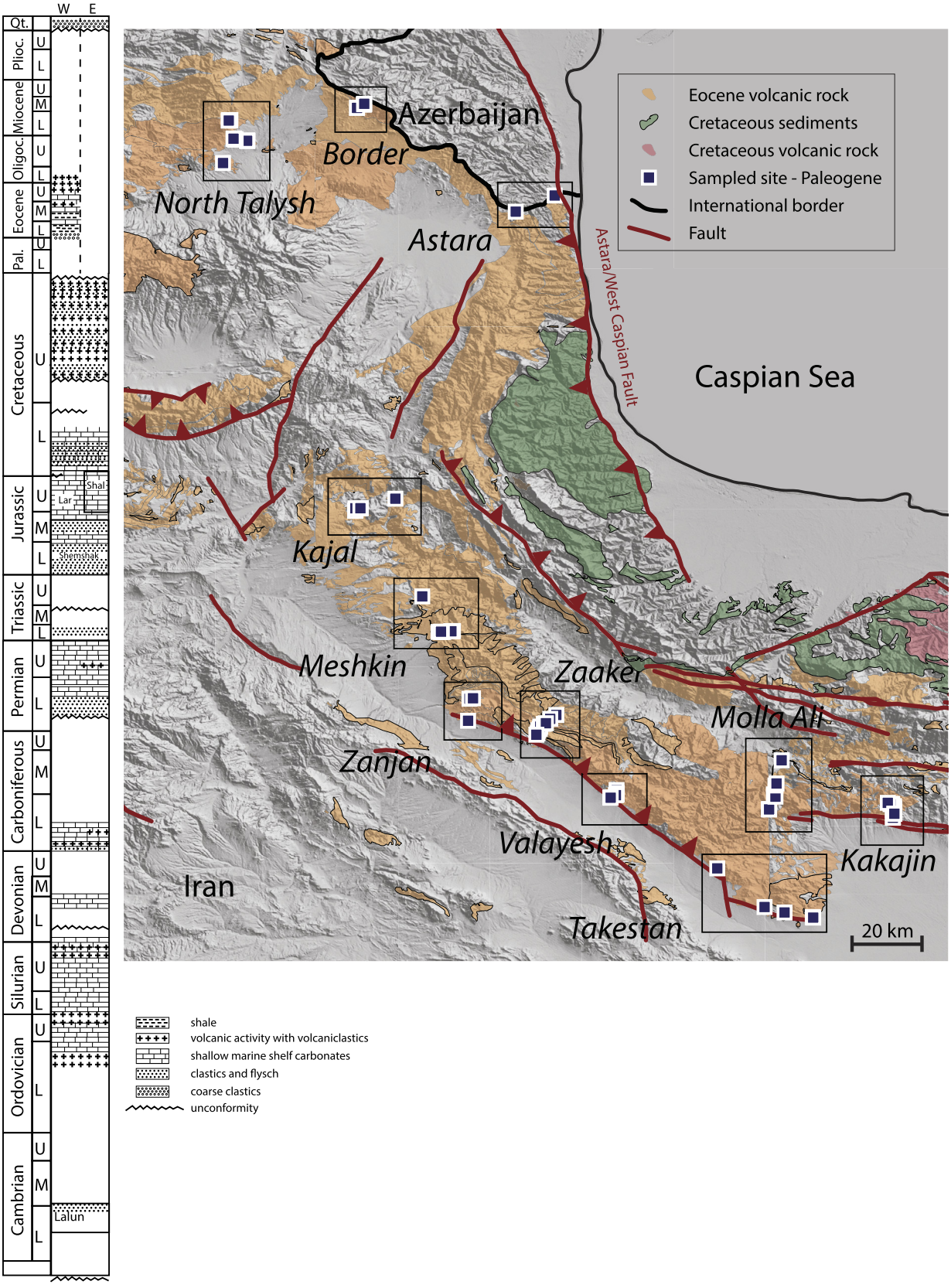

Fig. 2. Map of the Talysh with sampled paleomagnetic sites and localities and stratigraphic column (modified after Berberian and King, 1981).

genic magnetometer equipped with three DC SQUIDS (noise level 3×10^{-12} A m^2) for thermal demagnetization, or with a robotized 2G DC-SQUID magnetometer (dynamic range 3×10^{-12} to 5×10^{-5} A m^2) for AF demagnetization. Most samples show decreasing magnetization up to temperatures of 550–580 °C, indicative of (Ti-poor) magnetite. Some samples required higher temperatures up to 680 °C, indicative of the presence of hematite. The results were analyzed using orthogonal vector diagrams and

the characteristic remanent magnetization (ChRM) directions were determined using principal components analysis. Great circle analysis was performed on samples that had components that were not entirely removed after demagnetization, or became viscous or spurious at higher temperatures. The mean directions were determined using standard Fisher statistics, and a 45° cut-off was used. Per site (flow) the 95% cone of confidence (α_{95}) was determined, while for a sequence of flows errors in declination (ΔD_x) and inclination (ΔI_x) were calculated from the A95 of the VGP distribution. We used the criteria of Deenen et al. (2011), which means we determine A95 of the VGP distribution, and require the value to be between the N-dependent values of $A95_{min}$ and $A95_{max}$ to represent paleosecular variation (PSV). We used the web portal Paleomagnetism.org for the interpretation of demagnetization diagrams and for assessing the statistical properties of directional distributions (all appropriate references are given in the portal). This is an open source and platform independent on-line application (Koymans et al., 2016). We provide all data and interpretations in the online supplementary information in files that can simply be imported into the portal. Where possible, bedding planes were measured in the field, and we give our paleomagnetic results both before tilt correction (geographic coordinates, NOTC) and after tilt correction (tectonic coordinates, TC). However, for volcanic rocks, often no clear bedding could be observed. In these cases we estimated bedding from geological maps (1:100.000 series and 1:250.000 series, Geologic Survey of Iran) and/or Google Earth. All drilling directions and bedding were corrected for a declination of 4.6° according to the International Geomagnetic Reference Field (IGRF).

All demagnetization diagrams with interpreted directions are included in the appendix as *Site*.dir files. These files can be opened in the interpretation portal of Paleomagnetism.org under Advanced Options, and Import Application Save. All individual sites are imported into the Statistics portal, where they can be combined, viewed and assessed per locality or in any other combination desired. We provide all sites per locality as *Locality*.pmag files, which can be opened in the statistics portal of Paleomagnetism.org, in a way identical to the Interpretation portal.

4. Results

Sites of Eocene rocks that were geographically close together were grouped into 11 localities (Fig. 2). Demagnetization behavior of the samples is mostly straightforward, with no significant low coercivity/low temperature components. Representative examples of demagnetization diagrams and site averages are shown in Fig. 3. In general, the component above 20 mT or above 200 °C was interpreted. Samples showing partially unresolved components after demagnetization were interpreted using great-circle analysis (McFadden and McElhinny, 1988). For these samples, often the steps below 20 mT or 200 °C were taken into account. As a rule, we accepted only sites where the number of setpoints (i.e. directly interpreted ChRM components) was equal or greater than the number of great circle solutions (Fig. 3G). If there were not enough setpoints, we combined two nearby sites with a CTMD to obtain enough set points to perform the great-circle analysis. Results of all sites per locality are shown in Fig. 4.

Astara

In the Astara locality there are only two sites, CH88 and IR04. CH88 is the site that was dated in the study of Chiu et al. (2013). We were unable to find the basalt that was mentioned in the study and sampled a tuff breccia. Paleomagnetic results of this site only show low temperature components. Above ∼30 mT or 300 °C, the samples show 'spaghetti plot' behavior. This site is therefore omitted. The other site that was sampled at this locality, IR04, is an extrusive volcanic rock. Although it shows a clockwise rotation after tilt correction, the inclination is anomalously low. As we only have sampled one flow, we are not able to determine the average direction from this locality and dismiss it for further interpretation.

Border

The Border locality consists of 7 sites, of which 2 are sedimentary rocks. Sites IR100, 101 and 102 show a small cluster with different directions than site IR103-106. They show no rotation in tectonic coordinates, versus a rotation of about 20 degrees clockwise in geographic coordinates, so it is unlikely that these sites have a present day field overprint. Also, they have shallow inclinations in geographic coordinates (NOTC), versus steeper inclinations in tectonic coordinates (TC). We have inverted IR104 to normal polarity (but with a negative inclination), while IR103 and IR106 have anomalous south-down directions and fall outside the 45° cut-off.

North Talysh

The North Talysh locality consists of 26 sites, of both normal and reversed polarity. Inclinations are generally shallow, and become steeper after tectonic correction (TC). If we invert all reversed sites to normal, no sites are rejected on the basis of the 45° cut-off, but we reject 7 sites on the basis of too high internal dispersion ($k < 50$, Table 1), although the means of $N = 26$ and $N = 19$ are identical within errors (ΔD_x, ΔI_x). The mean declination of the remaining sites ($N = 19$) does not significantly change upon tilt correction (from ∼29° to ∼30°), while the mean inclination increases significantly (from ∼23° to ∼37°). A95 values are within the required $A95_{min}$–$A95_{max}$ envelope and hence the locality likely represents PSV, although a reversal test is negative.

Kajal

The Kajal locality consists of 6 sites and has only normal directions. IR98 is an Oligocene trachybasalt/trachyandesite (1:100.000 series geologic maps, Geologic Survey of Iran). Directions however are very similar to the other sites of reported Eocene age. The mean declination does not change upon tilt correction (∼28°), while the mean inclination decreases (from ∼50° to ∼39°) but still within error since $\Delta I_x = 13.1°$ after tilt correction.

Meshkin

The Meshkin locality consists of 10 sites all sites having normal polarities. Two sites (IR59 and IR63) were rejected ($k < 50$, Table 1) although all sites fall within the 45° cut-off. The mean declination changes upon tilt correction (from ∼20° to ∼29°), while the mean inclination increases (from ∼40° to ∼52°). A95 values are within the required $A95_{min}$–$A95_{max}$ envelope.

Zanjan

The Zanjan locality consists of 3 sites. All sites show normal polarity and have very low inclinations in geographic coordinates that become steeper in tectonic coordinates (from ∼31° to ∼41°). The mean declination changes slightly upon tilt correction (from ∼11° to ∼17°). One site (IR18) has $k = 42$ but this is a realistic value for (tuffaceous) sedimentary rocks.

Zaaker

The Zaaker locality consists of 9 sites. Sites IR69 and IR73 show an anomalous direction and fall outside the 45° cut-off. In addition, IR73 is not fully demagnetized at 100 mT, caused by the presence of hematite, but samples are fully thermally demagnetized at a temperature of 680 °C. IR67 and IR68 show anomalous declinations but have very low k values and are rejected, while also IR20 and IR71 have $k < 50$. The sites show greater dispersion after tilt correction, providing a negative fold test. Hence, only three sites of this locality are left that meet our criteria.

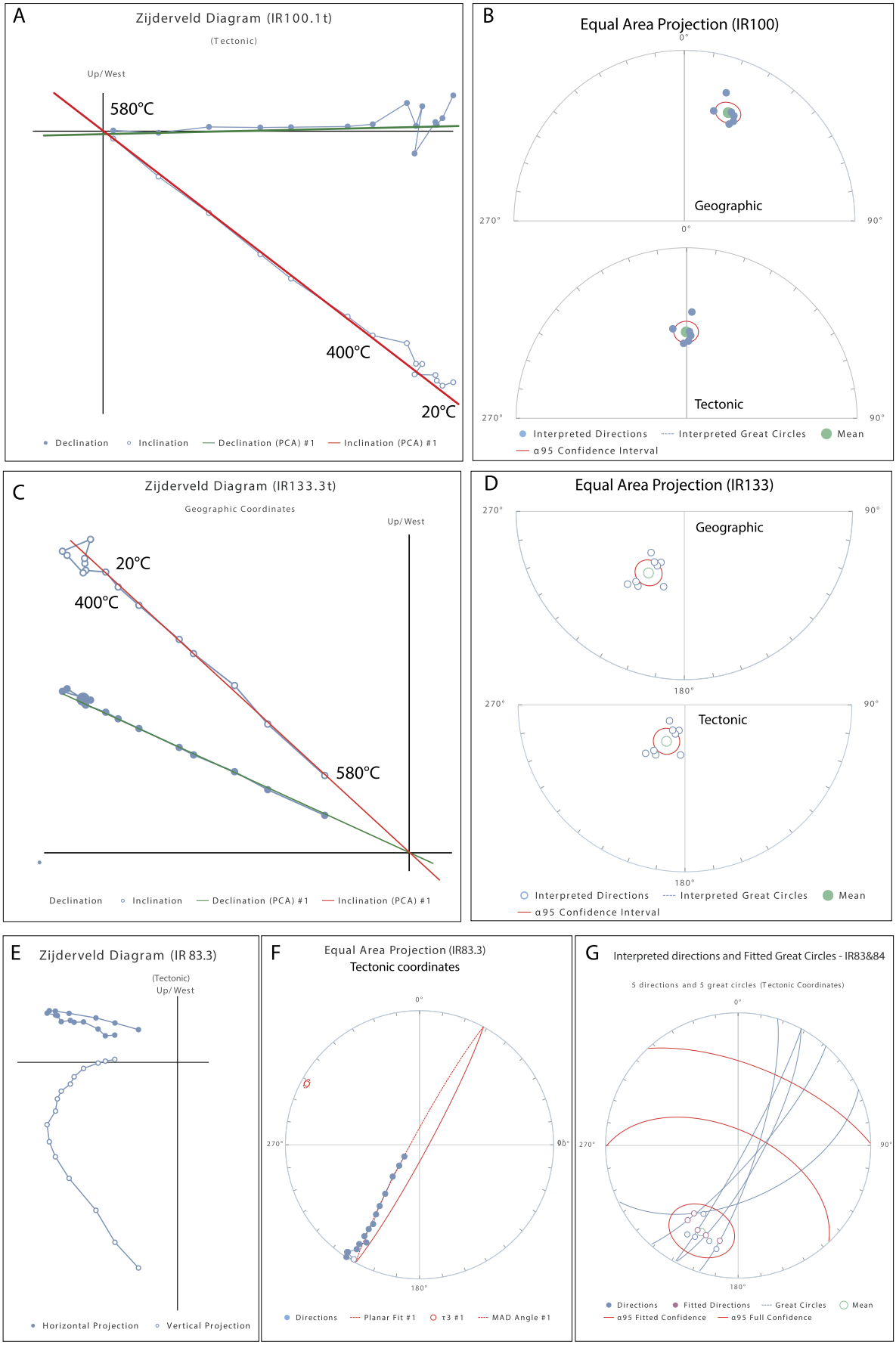

Fig. 3. Examples of paleomagnetic results and interpreted directions. Zijderveld diagrams (Figs. 3A, 3C and 3E), equal area projections of directions of one site (Figs. 3B, 3D and 3G), great-circle interpretation of a sample (Fig. 3F) and great-circle solutions and directions of one site (Fig. 3G).

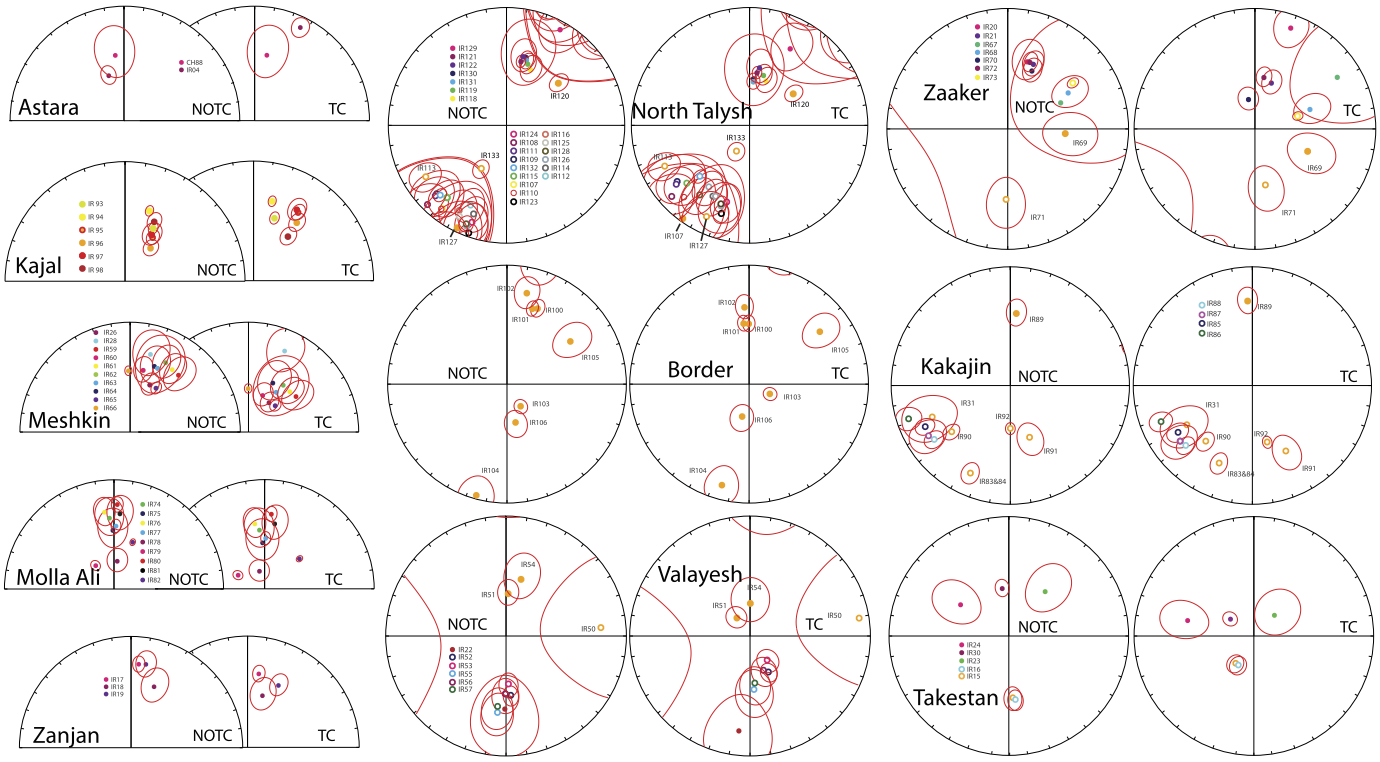

Fig. 4. Equal area projections of site means per locality. NOTC is before tilt correction (geographical coordinates), TC is after tilt correction (tectonic coordinates).

Valayesh

The Valayesh locality consists of 9 sites, in which both normal and reversed polarities are present. IR22 ($k = 13$) and IR50 ($k = 7$) are rejected because of both low k values and falling outside the 45° cut-off. Also IR54 and IR56 are rejected because $k < 50$ (Table 1). Both in geographic and tectonic coordinates the declinations show – within error (resp. $\Delta D_x = 11.4°$ and $\Delta D_x = 21.9°$) – no significant rotation with respect to North. Inclinations become steeper upon tectonic correction (from ∼49° to ∼64°).

Takestan

The Takestan locality consists of 5 sites. Both normal and reversed polarities are observed. Site IR23 is rejected ($k < 50$, Table 1), and the remaining sites are very scattered. The mean declination in geographic coordinates shows no significant rotation with respect to North, similar to Valayesh. Upon tilt correction the scatter increases ($A95 > A95_{max}$) and the directional distribution is meaningless.

Molla Ali

The Molla Ali locality consists of 9 sites, all showing normal polarities and all sites having high k values. Like Valayesh (and Takestan in geographic coordinates), declinations show no significant rotation with respect to North, both before and after tilt correction, while inclinations become steeper upon correction (from ∼45° to ∼51°). After tilt correction, only site IR79 falls outside of the 45° cut-off.

Kakajin

The Kakajin locality consists of 11 sites, of which two (IR83 and IR84) are taken together, thus we calculate k values for 10 sites. Some samples of sites IR83 and IR84 contain an unremoved component, which is interpreted using great-circle analysis (Fig. 4G). To have enough set points for the great-circle analyses, these sites were taken together. This locality has mostly reversed directions, with the exception of IR89. IR91 and IR92 are located close to each other and both show anomalous directions that are rejected by the 45° cut-off. IR87 is rejected because of $k < 50$ (Table 1). Of the remaining 7 sites, the mean inclination does not change within error upon tilt correction (from ∼28° to ∼31°). The mean declination changes slightly upon tilt correction (from ∼50° to ∼43°), and this locality shows therefore a larger than average rotation, compared to most other sites.

5. Discussion

5.1. Paleomagnetic directions

In general, the results of our sites are good to excellent, most sites (80%) met our criterion of low dispersion of the distribution ($k > 50$), denoting that these are good recorders of the geomagnetic field. Low values ($k < 50$) are typically expected for sedimentary rocks, and some 10% of our sites were in volcaniclastic rocks. These sites are expected to give low k values if they are epiclastic, i.e. deposited through reworking of volcanic material, relatively slowly and at low temperatures. In other cases, where volcaniclastic deposits such as ignimbrites, debris avalanches, hyalotuffs or peperites are present, deposition can take place within minutes to hours, at high temperatures. Considering the unusually high (up to $k = 300$) values of our sedimentary rock sites, it is likely that our sampling mainly included pyroclastic rocks that were deposited at higher temperatures. Indeed, some geologic maps mention the presence of units containing autoclastic and hyaloclastic breccias and tuffs and pyroclastic rocks.

Approximately 20% of our sites did not meet our criterion of $k > 50$, which is acceptable for sediments but not for single cooling units. After Eocene extrusive volcanism ended, a pulse of intrusive activity started, which intruded into the Eocene volcanic succession. The intrusives were mainly emplaced from the Late Eocene up to the Miocene. Intrusive bodies have formed a major role in hydrothermal metasomatism and resulting mineralization. Eocene

Table 1
List of sampled sites with location, lithology and results.

Name	Locality	Latitude	Longitude	*N*	*k*	a95	Dec (NOTC)	Inc (NOTC)	Dec (TC)	Inc (TC)	Bedding strike	dip	Lithology (field)	Unit (100k map)	100k map	Age	Reference	Stage
CH88	Astara	38.39232	48.65777	6	25	13.8	352.5	42.0	10.5	41.4	360	20	Tuffbreccia	Kuv	Astara	45.3 Ma	Chiu et al., 2013	Lutetian
IR004	Astara	38.44547	48.78607	5	167	5.9	341.4	55.9	26.0	10.3	330	70	Megaporphyritic Andesite-latite	Pevt	Astara	Paleocene		
IR100	Border	38.73457	48.13535	6	151	5.5	22.0	32.1	359.7	48.0	160	30	Lava flow	Epa2	Razi	Eocene		
IR101	Border	38.73457	48.13535	6	191	4.9	18.5	33.6	354.8	47.6	160	30	Lava flow	Epa3	Razi	Eocene		
IR102	Border	38.73429	48.13530	4	124	8.3	12.2	22.8	356.6	35.6	160	30	Lava flow	Epa3	Razi	Eocene		
IR103	Border	38.74500	48.15763	7	177	4.5	148.5	72.2	115.3	74.4	300	10	Tuff breccia	Ev	Razi	Eocene		
IR104	Border	38.74585	48.15819	5	63	9.7	195.4	3.4	195.0	13.1	300	10	Tuff breccia	Ev	Razi	Eocene		
IR105	Border	38.74642	48.15885	3	102	12.3	55.9	36.1	53.4	27.0	300	10	Welded tuffbreccia	Ev	Razi	Eocene		
IR106	Border	38.74778	48.15899	9	39	8.4	167.5	63.0	192.1	67.3	200	12	Lava flow	Ev	Razi	Eocene		
IR093	Kajal	37.40682	48.12985	14	144	3.3	27.9	48.6	18.4	44.2	229	10	Lava or welded tuff	Et	Hashtjin	Eocene		
IR094	Kajal	37.40659	48.12921	8	301	3.2	19.1	37.9	13.2	32.4	229	10	Redbeds	Et	Hashtjin	Eocene		
IR095	Kajal	37.41470	48.12993	18	69	4.2	32.2	54.5	33.1	32.5	305	22	Fine grained volcaniclastic sediments	Et	Hashtjin	Eocene		
IR096	Kajal	37.41495	48.14776	10	89	5.1	37.6	61.5	36.6	39.5	305	22	Andesite	Et	Hashtjin	Eocene		
IR097	Kajal	37.41485	48.14641	7	78	6.9	29.7	53.2	31.3	31.3	305	22	Red and grey sediments	Et	Hashtjin	Eocene		
IR098	Kajal	37.44623	48.26146	3	602	5.0	26.1	43.9	37.9	51.5	67	13	Andesitic lava flow	Olv2	Hashtjin	Oligocene		
IR031	Kakajin	36.42003	49.89987	3	74	14.5	248.0	−30.0	239.0	−36.1	220	15	Tuffbreccia	E6an-ba	Takestan	Eocene		
IR083	Kakajin	36.39511	49.89958	10	70	5.8	204.4	−20.1	203.1	−29.7	130	10	Dark grey basalt	E6an-ba	Takestan	Eocene		
IR084	Kakajin	36.39483	49.89951			together	with IR83				130	10	Dark grey basalt	E6an-ba	Takestan	Eocene		
IR085	Kakajin	36.42505	49.90437	6	113	6.3	244.1	−21.7	237.7	−27.1	220	15	Porphyritic andesite	E6an-ba	Takestan	Eocene		
IR086	Kakajin	36.42505	49.90437	5	108	7.4	251.8	−11.1	248.4	−18.7	220	15	Porphyritic andesite	E6an-ba	Takestan	Eocene		
IR087	Kakajin	36.43306	49.90337	5	48	11.2	238.3	−20.5	232.3	−24.4	220	15	Tuff breccia	E6an-ba	Takestan	Eocene		
IR088	Kakajin	36.44063	49.89701	5	101	7.6	234.6	−22.7	228.0	−25.7	220	15	Basaltic lava	E6an-ba	Takestan	Eocene		
IR089	Kakajin	36.43935	49.89172	5	75	8.9	4.8	39.0	356.8	29.5	220	15	Basaltic lava	E6an-ba	Takestan	Eocene		
IR090	Kakajin	36.44385	49.88272	5	156	6.2	231.7	−37.4	219.9	−38.9	220	15	Basaltic lava	E6an-ba	Takestan	Eocene		
IR091	Kakajin	36.40798	49.90458	5	74	8.9	159.6	−51.6	153.0	−38.1	220	15	Reddish andesitic lava flow	E6an-ba	Takestan	Eocene		
IR092	Kakajin	36.40798	49.90430	5	370	4.0	179.9	−60.5	165.4	−49.3	220	15	Grey andesitic lava flow	E6an-ba	Takestan	Eocene		
IR026	Meshkin	37.00705	48.40358	6	101	6.7	22.6	51.7	34.9	63.5	85	14	Trachyandesite with large phenocrysts	Eab	Hashtjin	Eocene		
IR028	Meshkin	37.12424	48.35010	3	117	11.4	14.6	27.6	23.9	20.3	0	22	Andesite	Etl1	Hashtjin	Eocene		
IR059	Meshkin	37.01016	48.45117	8	23	11.9	40.3	32.7	53.2	45.2	85	20	Tuff	Ev2	Hashtjin	Eocene		
IR060	Meshkin	37.00926	48.44878	7	66	7.5	11.9	42.1	21.2	60.8	85	20	Porphyritic basalt	Ev2	Hashtjin	Eocene		
IR061	Meshkin	37.00909	48.44653	5	62	9.8	33.9	32.1	45.6	46.5	85	20	Porphyritic basalt	Ev2	Hashtjin	Eocene		
IR062	Meshkin	37.00936	48.44628	5	70	9.2	27.1	29.9	36.5	46.0	85	20	Porphyritic basalt	Ev2	Hashtjin	Eocene		
IR063	Meshkin	37.00931	48.44594	5	19	17.8	23.3	37.0	34.7	53.7	85	20	Porphyritic basalt	Ev2	Hashtjin	Eocene		
IR064	Meshkin	37.00683	48.41904	4	50	13.1	20.2	36.4	26.4	48.8	85	14	Porphyritic basalt	Eab	Hashtjin	Eocene		
IR065	Meshkin	37.00760	48.41446	6	294	3.9	30.5	51.8	45.3	62.1	85	14	Volcaniclastic red sediment	Eab	Hashtjin	Eocene		
IR066	Meshkin	37.00798	48.41171	5	522	3.4	358.4	43.6	359.5	57.6	85	14	Megaporphyritic basalt	Eab	Hashtjin	Eocene		

(*continued on next page*)

Table 1 (*continued*)

Name	Locality	Latitude	Longitude	*N*	*k*	a95	Dec (NOTC)	Inc (NOTC)	Dec (TC)	Inc (TC)	Bedding strike	dip	Lithology (field)	Unit (100k map)	100k map	Age	Reference	Stage
IR074	Molla Ali	36.42217	49.49193	3	94	12.8	356.4	35.3	355.0	45.2	95	10	Very fine grained lava or welded tuff	Ea4 (250k map)	Zanjan 250k	Eocene		
IR075	Molla Ali	36.42239	49.49189	3	74	14.4	358.9	45.4	357.5	55.4	95	10	Porphyritic basalt	Ea4 (250k map)	Zanjan 250k	Eocene		
IR076	Molla Ali	36.42279	49.49198	3	108	11.9	353.0	29.9	351.4	39.7	95	10	Very fine grained lava or welded tuff	Ea4 (250k map)	Zanjan 250k	Eocene		
IR077	Molla Ali	36.42300	49.49209	3	872	4.2	1.8	41.9	1.2	51.9	95	10	Very fine grained lava or welded tuff	Ea4 (250k map)	Zanjan 250k	Eocene		
IR078	Molla Ali	36.46414	49.51286	4	150	7.5	6.7	69.2	343.7	76.4	130	10	Very fine grained lava or welded tuff	E6v	Takestan	Eocene		
IR079	Molla Ali	36.47186	49.50750	5	401	3.8	322.1	67.9	297.2	67.8	130	10	Very fine grained lava or welded tuff	E6v	Takestan	Eocene		
IR080	Molla Ali	36.50113	49.51282	3	1095	3.7	2.2	23.6	5.2	32.0	60	10	Porphyritic andesite	Ev2	Jirandeh	Eocene		
IR081	Molla Ali	36.50766	49.51643	5	74	8.9	4.5	31.6	8.8	39.6	60	10	Porphyritic andesite	Ev2	Jirandeh	Eocene		
IR082	Molla Ali	36.58409	49.53320	11	275	2.8	21.2	51.2	3.7	40.2	225	20	Fine grained sediments	Es	Jirandeh	Eocene		
IR107	North Talysh	38.69389	47.71810	3	15	33.0	217.7	11.8	215.5	3.2	65	18	Basalt	Ebl	Lahrud	Eocene		
IR108	North Talysh	38.69369	47.71802	3	70	14.8	224.9	−5.8	227.5	−11.7	65	18	Basalt	Ebl	Lahrud	Eocene		
IR109	North Talysh	38.69378	47.71679	3	37	20.7	225.4	−18.4	232.1	−23.4	65	18	Basalt	Ebl	Lahrud	Eocene		
IR110	North Talysh	38.69378	47.71655	3	14	33.8	217.9	−11.1	222.3	−18.8	65	18	Basalt	Ebl	Lahrud	Eocene		
IR111	North Talysh	38.69359	47.71631	3	115	11.5	225.2	−16.2	231.1	−21.5	65	18	Basalt	Ebl	Lahrud	Eocene		
IR112	North Talysh	38.69326	47.71622	6	34	11.6	204.3	−42.1	220.8	−51.9	65	18	Basalt	Ebl	Lahrud	Eocene		
IR113	North Talysh	38.69311	47.71488	3	210	8.5	237.4	−20.1	244.3	−21.4	65	18	Basalt	Ebl	Lahrud	Eocene		
IR114	North Talysh	38.69302	47.71374	3	65	9.5	200.3	−20.9	207.3	−32.9	65	18	Basalt	Ebl	Lahrud	Eocene		
IR115	North Talysh	38.69280	47.71339	3	168	11.2	219.3	−21.8	227.2	−28.5	65	18	Basalt	Ebl	Lahrud	Eocene		
IR116	North Talysh	38.69251	47.71301	3	122	15.4	209.0	−18.5	215.6	−28.3	65	18	Basalt	Ebl	Lahrud	Eocene		
IR118	North Talysh	38.62611	47.77453	4	351	7.2	23.3	47.4	20.3	57.2	125	10	Dacite	Ea2p	Lahrud	Eocene		
IR119	North Talysh	38.62625	47.77411	4	56	7.1	19.1	44.3	15.6	53.8	125	10	Dacite	Ea2p	Lahrud	Eocene		
IR120	North Talysh	38.62625	47.77383	3	47	5.1	50.8	42.9	54.1	52.4	125	10	Dacite	Ea2p	Lahrud	Eocene		
IR121	North Talysh	38.62590	47.77340	3	44	4.3	12.7	43.8	8.0	52.9	125	10	Dacite	Ea2p	Lahrud	Eocene		
IR122	North Talysh	38.62593	47.77379	3	69	11.2	13.7	39.9	9.8	49.1	125	10	Dacite	Ea2p	Lahrud	Eocene		
IR123	North Talysh	38.63072	47.73427	3	1031	4.9	199.3	−3.6	197.7	−22.5	128	20	Lava flow	Edl	Lahrud	Eocene		
IR124	North Talysh	38.63067	47.73487	3	87	12.3	199.6	−13.8	196.6	−32.7	128	20	Lava flow	Edl	Lahrud	Eocene		
IR125	North Talysh	38.63072	47.73512	3	33	18.1	207.3	−14.2	205.5	−33.8	128	20	Lava flow	Edl	Lahrud	Eocene		
IR126	North Talysh	38.63050	47.73515	3	550	18.8	201.6	−9.3	199.6	−28.4	128	20	Lava flow	Edl	Lahrud	Eocene		
IR127	North Talysh	38.63031	47.73544	3	642	15.0	205.7	4.0	205.2	−15.6	128	20	Lava flow	Edl	Lahrud	Eocene		
IR128	North Talysh	38.63026	47.73568	3	297	3.8	202.2	−10.6	200.0	−29.8	128	20	Lava flow	Edl	Lahrud	Eocene		
IR129	North Talysh	38.63330	47.73049	3	305	13.3	29.2	7.8	27.9	27.4	130	20	Megaporphyritic lava flow	Epa	Lahrud	Eocene		
IR130	North Talysh	38.63335	47.72973	3	582	21.9	16.1	39.9	4.7	57.4	130	20	Megaporphyritic lava flow	Epa	Lahrud	Eocene		
IR131	North Talysh	38.63292	47.72921	4	457	5.3	17.0	41.9	5.0	59.5	130	20	Megaporphyritic lava flow	Epa	Lahrud	Eocene		
IR132	North Talysh	38.63280	47.72864	3	121	4.9	223.5	−19.6	224.2	−39.5	130	20	Megaporphyritic lava flow	Epa	Lahrud	Eocene		
IR133	North Talysh	38.55255	47.69409	8	77	6.4	210.2	−55.2	206.9	−70.1	125	15	Reddish lava	Epl	Lahrud	Eocene		

Table 1 (*continued*)

Name	Locality	Latitude	Longitude	*N*	*k*	a95	Dec (NOTC)	Inc (NOTC)	Dec (TC)	Inc (TC)	Bedding strike	dip	Lithology (field)	Unit (100k map)	100k map	Age	Reference	Stage
IR015	Takestan	36.06749	49.63571	6	139	5.7	176.3	−47.0	213.6	−67.6	55	30	Basaltic andesite	E6an	Takestan	35.8 Ma	Chiu et al., 2013	Priabonian
IR016	Takestan	36.06562	49.63717	6	136	5.8	174.1	−45.5	208.0	−67.5	55	30	Basaltic andesite	E6an	Takestan	Eocene		
IR023	Takestan	36.22788	49.32134	4	46	13.8	39.2	50.4	44.8	70.1	123	20	Porphyritic trachyandesite/latite	Ea6 (250k map)	Zanjan 250k	Eocene		
IR024	Takestan	36.10048	49.47698	3	82	13.7	303.0	50.3	283.2	42.7	135	20	Grey/purple porphyritic andesite	Ea6 (250k map)	Zanjan 250k	Eocene		
IR030	Takestan	36.08253	49.54280	3	365	4.8	352.1	57.1	305.9	70.4	120	25	Trachyandesite	Etr-an	Takestan	Eocene		
IR022	Valayesh	36.48612	48.98974	5	13	22.2	181.0	39.0	186.7	21.4	123	20	Trachybasalt	Eka	Soltaniyeh	Eocene		
IR050	Valayesh	36.47618	48.99030	4	7	38.5	84.9	−22.0	80.7	−9.0	123	20	Porphyritic trachyandesite/latite	Eka	Soltaniyeh	Eocene		
IR051	Valayesh	36.47314	48.99009	7	74	7.1	2.8	61.1	324.0	74.9	123	20	Tuffbreccia	Eka	Soltaniyeh	Eocene		
IR052	Valayesh	36.47210	48.98996	6	129	5.9	175.5	−48.9	153.1	−62.5	123	20	Tuffbreccia	Eka	Soltaniyeh	Eocene		
IR053	Valayesh	36.47289	48.99002	4	156	7.4	177.1	−57.1	144.6	−70.0	123	20	Tuffbreccia	Eka	Soltaniyeh	Eocene		
IR054	Valayesh	36.46910	48.98752	6	29	12.7	14.8	49.6	0.5	67.8	123	20	Tuffbreccia	Eka	Soltaniyeh	Eocene		
IR055	Valayesh	36.46166	48.96946	5	82	14.1	186.4	−36.1	175.8	−53.2	123	20	Ignimbrite	Eka	Soltaniyeh	Eocene		
IR056	Valayesh	36.46099	48.96982	4	44	8.5	180.6	−50.1	158.7	−65.0	123	20	Ignimbrite	Eka	Soltaniyeh	Eocene		
IR057	Valayesh	36.46075	48.97038	3	97	12.6	186.8	−40.6	174.3	−57.6	123	20	Ignimbrite	Eka	Soltaniyeh	Eocene		
IR020	Zaaker	36.67273	48.72948	6	45	10.1	16.2	41.6	19.5	12.2	300	30	Porphyritic andesite	Eka8	Tarom	Eocene		
IR021	Zaaker	36.73357	48.79146	8	63	7.0	21.6	41.9	19.7	56.8	117	15	Purple andesite	Ekk1	Tarom	Eocene		
IR067	Zaaker	36.68324	48.73213	2	26	50.6	63.7	49.6	57.8	20.6	315	30	Andesite	Eka5	Tarom	Eocene		
IR068	Zaaker	36.68824	48.73705	8	28	10.6	59.1	41.3	70.5	50.1	103	14	Tuffaceous sediments	Eka5	Tarom	Eocene		
IR069	Zaaker	36.69500	48.73847	3	77	14.2	94.7	50.5	113.1	50.8	105	15	Andesite	Eka3	Tarom	Eocene		
IR070	Zaaker	36.70414	48.75034	5	104	7.6	22.6	46.8	347.7	69.7	139	30	Dark fine grained volcaniclastics	Ekk8	Tarom	Eocene		
IR071	Zaaker	36.72064	48.77127	5	41	12.1	181.4	−41.1	169.4	−50.9	135	15	Andesite	Ekk2	Tarom	Eocene		
IR072	Zaaker	36.70624	48.75715	12	65	5.4	18.4	41.4	9.9	54.3	135	15	Dark fine grained volcaniclastics	Ekk3	Tarom	Eocene		
IR073	Zaaker	36.66836	48.72574	5	501	3.4	54.7	−34.4	73.2	−59.8	300	30	Andesite	Eka5	Tarom	Eocene		
IR017	Zanjan	36.71437	48.50094	12	70	5.2	5.2	25.7	8.7	33.7	60	10	Andesite and tuffbreccia	E8a	Tarom	Eocene		
IR018	Zanjan	36.78695	48.50551	8	42	8.6	20.6	41.1	16.0	50.1	135	10	Tuffaceous sediments	Eka1	Tarom	Eocene		
IR019	Zanjan	36.78844	48.51714	7	89	6.4	10.1	24.9	26.4	37.9	44	29	Red andesite	Eka1	Tarom	Eocene		

tuffites and volcanic rocks are affected by extensive metasomatism and scattered vein mineralization (Ghorbani, 2013). Hydrothermal alteration might be a possible explanation for the low k values that we find in some volcanic rocks, as they could result in (partial) overprints. Nonetheless, if we include also sites with $k < 50$, the result is identical within errors (ΔD_x, ΔI_x). Applying the tilt corrections increases the inclination significantly by some 10°, but does not significantly change the declination and thus the rotation (Table 2). Inclinations are generally too shallow, even after tilt correction. This is a much reported problem for Eocene rocks (e.g. Si and Van der Voo, 2001), for which yet no plausible explanation is found.

5.2. North Takestan lineament

The Talysh mountains show an abrupt shift near Takestan: the southern edge of the Alborz jumps approximately 40 km northward, over a roughly north–south trending line. Although there is no major fault drawn on any map, this lineament is sometimes mentioned as the North Takestan fault, or Takestan–Rasht fault (e.g. Azizi and Moinevaziri, 2009). The Molla Ali locality is relatively close to this inferred fault, at roughly 5 km distance, and thus could be affected by movement along the fault. Hence, we decided to use only the 6 northern localities as representative for the Talysh mountains, north of Valayesh since the southern 4 localities may have been affected by regional tectonics. Nonetheless, our strict criteria do not make a significant difference for the amount of rotation, as mean declinations are similar for 10 localities and 6 localities (Fig. 5). Averaging all site means of the 6 northern localities gives a mean declination $D \pm \Delta D_x = 25.9 \pm 6.1°$ for the Talysh Mountains of NW Iran.

5.3. Literature data

We complement our new data set with previous paleomagnetic work from the Eastern Pontides to the Lesser Caucasus region (see the compiled data and corresponding references in Table A1). Paleomagnetic data in the Eastern Pontides – Lesser Caucasus – Talysh – Alborz region was grouped based on the geology and geometry (like strike trend) into coherent domains. Based on coherent paleomagnetic results and geometry, we define coherently rotating domains based on our paleomagnetic data (and thus are a simplification of the true deformation history). Two of our domains are within the Eastern Pontides region of Turkey, but for the sake of clarity we call the most eastern one the Eastern Pontides domain, and the other the Pontides domain. We then distinguish five domains: the Pontides, the Eastern Pontides, the Lesser Caucasus, the Talysh and the Alborz (Fig. 6). The new data from our study are taken as representative for the Talysh domain. These data are consistent with the results of Cifelli et al. (2015), who report a mean declination of 23.4° for the post-Eocene of the western limb of the Alborz Mountains. The expected declination from the Eurasia apparent polar wander path for Eocene rocks is around 10 degrees, for the whole region from the Pontides to the Central Alborz (Torsvik et al., 2012). Thus, rotations were calculated with respect to this expected declination. In addition, we recalculated all mean directions to the average location 41°N, 45°E, which we use as a reference point. For the Pontides, Eastern Pontides and Lesser Caucasus domains, we parametrically resampled published data in Paleomagnetism.org (see Table A1). We only took data of Eocene age, from localities that were accepted in the review of Meijers et al. (2015; and references therein), and subsequently calculated the means of all resampled data per domain (Table 2). The file Eocene_directions_literature.pmag contains paleomagnetic data from the Pontides, Eastern Pontides and Lesser Caucasus that were previously published (see Table A1 for details). We do not use data from the South Armenian block, as this block is located south of a Cretaceous–Eocene suture. The SAB is the indentor with respect to the orocline, and may have undergone local or regional rotations due to collision.

For the Pontides domain, only two Eocene localities were obtained from limestones and volcanic rocks. For the Eastern Pontides domain, three localities consisting of volcanic and volcaniclastic deposits were used. Considering the relatively small amount of Eocene paleomagnetic directions in the Eastern Pontides of Turkey, future studies are expected to improve the estimates provided in this study. The Lesser Caucasus has many more sites, a total of 26 accepted localities, with mostly volcanic and volcaniclastic deposits and some turbiditic sedimentary rocks (Meijers et al., 2015).

We performed an orocline test averages for the Pontides, Eastern Pontides, Lesser Caucasus and Talysh blocks (Eastern Alborz of Cifelli et al., 2015 is within error the same), which results in a slope of 0.655, with a Pearson's ρ of 0.997. This indicates that about 65% of the rotations can be explained by post-Eocene curvature. This slightly more than the 50% post-Eocene curvature of the study of Meijers et al. (2015), which is probably caused by not taking into account the data of the SAB in our reconstruction.

5.4. Quantifying Arabia–Eurasia convergence

We estimate the amount of convergence accommodated in the Greater Caucasus fold-thrust belt from a first-order map view restoration back to 35 Ma. Paleomagnetically coherent blocks as determined above were drawn based on the position of paleomagnetic sites and tectonic boundaries. Our reconstruction assumes that the eastern Alborz and the Pontides were not moving relative to Eurasia since the late Eocene. There is evidence for thrusting to the north of these domains, e.g. in the South Caspian Basin (Hollingsworth et al., 2008), and our convergence estimates are therefore minimum values required to explain the paleomagnetic constraints. Furthermore, purely northward motions not resulting in rotations cannot be accounted for in this approach. The Arabia–Eurasia collision has caused deformation of tectonic blocks, which the GPlates reconstruction does not account for. However, it is known that Iran has shortened due to the Arabia–Eurasia collision (e.g. Mouthereau et al., 2012 and references therein). In our reconstruction at 35 Ma, Central Iran is thus drawn in up to the Neotethys suture zone as defined in GPlates. However, as it is a relatively unexplored region, not all deformation of blocks is well constrained. Thus, reconstructing the rotation of newly defined rigid blocks relative to each other often results in overlap of blocks or gaps between blocks. Our reconstruction is subsequently tested using the paleomagnetic constraints. For this, we use an iterative approach, in which we determine total Euler reconstruction poles from 0–35 Ma of each block relative to Eurasia (Table A3). We then use these Euler rotations to predict the Global Apparent Polar Wander Path (GAPWaP) of Torsvik et al. (2012) in the coordinates of each domain, (Table A2) using a thereto designed tool on Paleomagnetism.org (Li et al., 2017). We then iteratively update our reconstruction until the paleomagnetic data overlap with the polar wander paths as predicted by the reconstruction, and a geometrically and kinematically coherent result (at 35 Ma) is obtained (Fig. 7).

Our reconstruction shows that, to fulfil the paleomagnetic constraints on regional vertical axis rotations, a minimum of ~120 km of convergence must have been accommodated north of the Talysh (Fig. 6). North of the Eastern Pontides and the Lesser Caucasus, a minimum of 200–280 km convergence must be accommodated, which constrains the amount of convergence accommodated within the Caucasus orogeny. This sharp difference in Caucasus convergence between the Lesser Caucasus and Talysh (Fig. 6) re-

Table 2
Combined results of 10 and 6 localities of the Talysh and average results per domain. Data from the Alborz domain is from one study (Cifelli et al., 2015), while the other domains consist of data from multiple studies (for details see Table A1).

# Localities			N	N_{45}	Dec	Inc	R	k	α_{95}	K	A95	$A95_{min}$	$A95_{max}$	ΔD_x	ΔI_x	λ
10	$k > 50$	tc	74	65	22.2	44.2	60.1	13.2	5.0	12.5	5.2	2.3	5.9	5.8	6.6	25.9
		notc	74	67	20.3	36.4	62.4	14.3	4.7	16.9	4.3	2.2	5.8	4.6	6.4	20.3
10	all	tc	94	82	26.2	43.8	75.2	11.8	4.7	11.4	4.8	2.1	5.1	5.4	6.2	25.6
		notc	94	85	23.5	36.4	78.7	13.3	4.4	15.2	4.1	2.0	5.0	4.3	6.0	20.2
6	***k* > 50**	**tc**	**47**	**44**	**25.9**	**41.3**	**41.1**	**14.9**	**5.8**	**16.6**	**5.4**	**2.6**	**7.6**	**6.0**	**7.3**	**23.7**
		notc	47	44	24.9	31.9	41.5	17.4	5.3	26.8	4.2	2.6	7.6	4.4	6.7	17.3
6	all	tc	61	57	28.3	40.5	52.8	13.4	5.3	14.8	5.1	2.4	6.4	5.5	6.9	23.1
		notc	61	57	26.8	32.1	53.5	16.0	4.9	22.9	4.0	2.4	6.4	4.2	6.3	17.4

Geographic Coordinates

Site Name	N	N_{45}	Dec	Inc	k	α_{95}	l	R	K	R_{VGP}	A95	$A95_{min}$	$A95_{max}$	cut	S	ΔD_x	ΔI_x	minPalat	maxPalat	latitude	longitude	age	min age	max age
Eastern Pontides	63	63	330.8	38.4	29.1	3.4	21.7	60.9	32.0	61.1	3.2	2.3	6.0	45.0	14.4	3.5	4.6	18.6	25.0	41.60	41.80	35	33.9	56
Alborz	216	213	23.4	35.5	9.4	3.3	19.6	190.4	13.6	197.4	2.7	1.4	2.8	45.0	22.3	2.9	4.1	17.0	22.4	35.50	52.00	35		
Pontides	93	93	344.3	35.8	45.0	2.2	19.8	91.0	61.4	91.5	1.9	2.0	4.7	45.0	10.4	2.0	2.8	18.0	21.7	40.40	39.90	35	33.9	56
Lesser Caucasus	1213	1177	355.2	51.3	22.8	0.9	32.0	1125.4	20.3	1119.1	0.9	0.7	1.0	45.0	18.1	1.1	1.0	31.0	32.9	41.00	45.00	35	33.9	56
Talysh	47	44	24.9	31.9	17.4	5.3	17.3	41.5	26.8	42.4	4.2	2.6	7.6	45.0	15.8	4.4	6.7	13.3	21.8	37.50	48.50	35	33.9	56

Tectonic Coordinates

Site Name	N	N_{45}	Dec	Inc	k	α_{95}	l	R	K	R_{VGP}	A95	$A95_{min}$	$A95_{max}$	cut	S	ΔD_x	ΔI_x	minPalat	maxPalat	latitude	longitude	age	min age	max age
Eastern Pontides	63	63	330.8	38.4	29.1	3.4	21.7	60.9	32.0	61.1	3.2	2.3	6.0	45.0	14.4	3.5	4.6	18.6	25.0	41.6	41.8	35	33.9	56
Alborz	216	213	23.4	35.5	9.4	3.3	19.6	190.4	13.6	197.4	2.7	1.4	2.8	45.0	22.3	2.9	4.1	17.0	22.4	35.5	52	35		
Pontides	93	93	344.3	35.8	45.0	2.2	19.8	91.0	61.4	91.5	1.9	2.0	4.7	45.0	10.4	2.0	2.8	18.0	21.7	40.4	39.9	35	33.9	56
Lesser Caucasus	1213	1177	355.2	51.3	22.8	0.9	32.0	1125.4	20.3	1119.1	0.9	0.7	1.0	45.0	18.1	1.1	1.0	31.0	32.9	41	45	35	33.9	56
Talysh	47	44	25.9	41.3	14.9	5.8	23.7	41.1	16.6	41.4	5.4	2.6	7.6	45.0	20.1	6.0	7.3	18.6	29.6	37.5	48.5	35	33.9	56

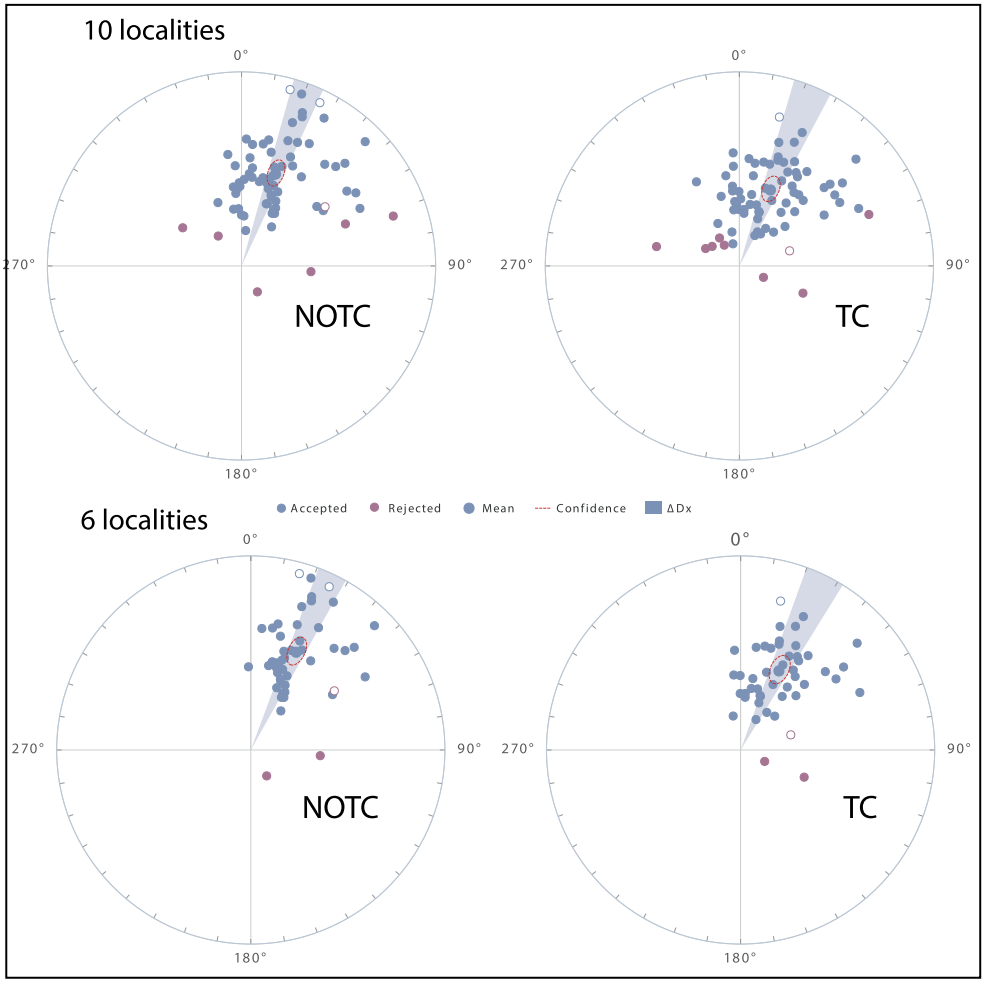

Fig. 5. Averages of all sites for 6 and 10 localities.

quires that a large dextral transform fault existed between the Anatolian and Iranian domains after the late Eocene. Barrier et al. (2008) already suggested the existence of such a fault since the early Eocene, which may coincide with the ancient plate boundary bounding the Iranian Cimmerides in the west. The difference in convergence would likely result in differences of accommodation in the Greater Caucasus. Indeed, there appear to be real and significant differences between various aspects of western and eastern Greater Caucasus including crustal structure, potential timing of exhumation and possible amounts of shortening. (e.g. Cowgill et al., 2016; Ershov et al., 2003; Forte et al., 2014; Mumladze et al., 2015). Our reconstruction provides the first quantitative estimate that this fault zone may have accommodated as much as 160 km of right-lateral, post-late Eocene slip. We hypothesize that the Arax fault is a present-day remnant of this transform fault, although this fault is believed to be left-lateral (see Fig. 1).

Our estimate is based on paleomagnetic data, and the 120–280 km post-Eocene convergence in the Caucasus is an independent corroboration of previous estimates based on seismological observations (Mumladze et al., 2015), who interpreted a slab-like body below the Greater Caucasus of up to 280 km down-dip length. Furthermore, our reconstruction is reasonably consistent with the estimate of Cowgill et al. (2016), who suggested, based on sediment provenance data, that an ocean basin south of the western Greater Caucasus of as much as 350–400 km wide has closed.

If a minimum of 200–280 km of convergence was accommodated in the Caucasus subduction zone, north of the Eastern Pontides and the Lesser Caucasus (Fig. 6), then the rest of the 800–900 km of Arabia–Eurasia convergence (McQuarrie and van Hinsbergen, 2013) must have been accommodated to the south of the Lesser Caucasus in the East Anatolian plateau. South of the Talysh, a maximum of 780 km must have been partitioned over Iranian plateau shortening and subduction in the Zagros. Our estimate of convergence accommodated north of the Talysh may add an additional 120 km of overriding plate convergence to the estimate of McQuarrie and van Hinsbergen (2013), which may push the age of Arabia collision in northwest Iran a few million years back.

There is widespread debate on the timing of collision of Arabia with the Taurides, or the East Anatolian accretionary prism, with estimates ranging from as old as ∼50 Ma to as young as ∼5 Ma, and on how, when and where post-collisional convergence was accommodated (Cowgill et al., 2016; Hüsing et al., 2009; Okay et al., 2010; Rolland et al., 2012; Vincent et al., 2016). Our new constraint on the partitioning of convergence into the Caucasus realm now places quantitative constraints on the area that must have been consumed after 35 Ma to the south of the Lesser Caucasus and aids future studies that aim to determine how the remaining convergence was partitioned over subduction, plateau shortening, and extrusion. Obtaining further constraints on how much, when and where this convergence was accommodated using our paleomagnetic method combined with GPlates for quantitative reconstruction is very promising. Clearly, it is a very useful tool for the analysis of the effects of continent–continent collision on orogenesis, plateau rise, and extrusion.

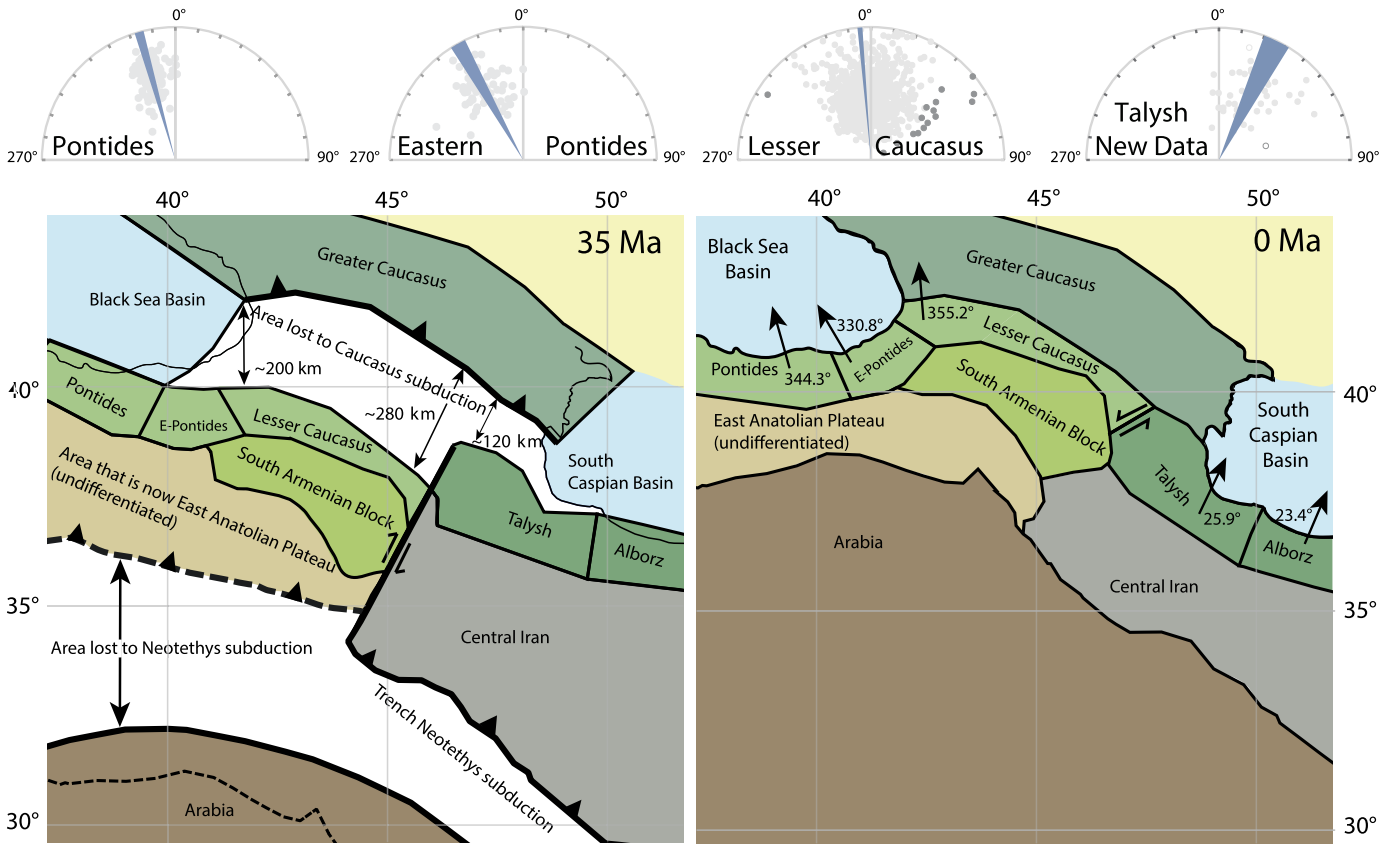

Fig. 6. Reconstruction of the Caucasus orocline and quantification of the partitioning of Arabia–Europe convergence between 35 Ma and 0 Ma. Modified GPlates reconstruction software output for our reconstruction at 0 Ma and 35 Ma, and averages for parametrically sampled paleomagnetic data for Pontides, Eastern Pontides, Lesser Caucasus and Talysh blocks. Data in dark grey fall outside of the cut-off and are rejected for calculation of the average. Open circles represent negative inclinations. Estimated total reconstruction poles at 35 Ma relative to Eurasia for the segments or the orocline are given in Appendix A3.

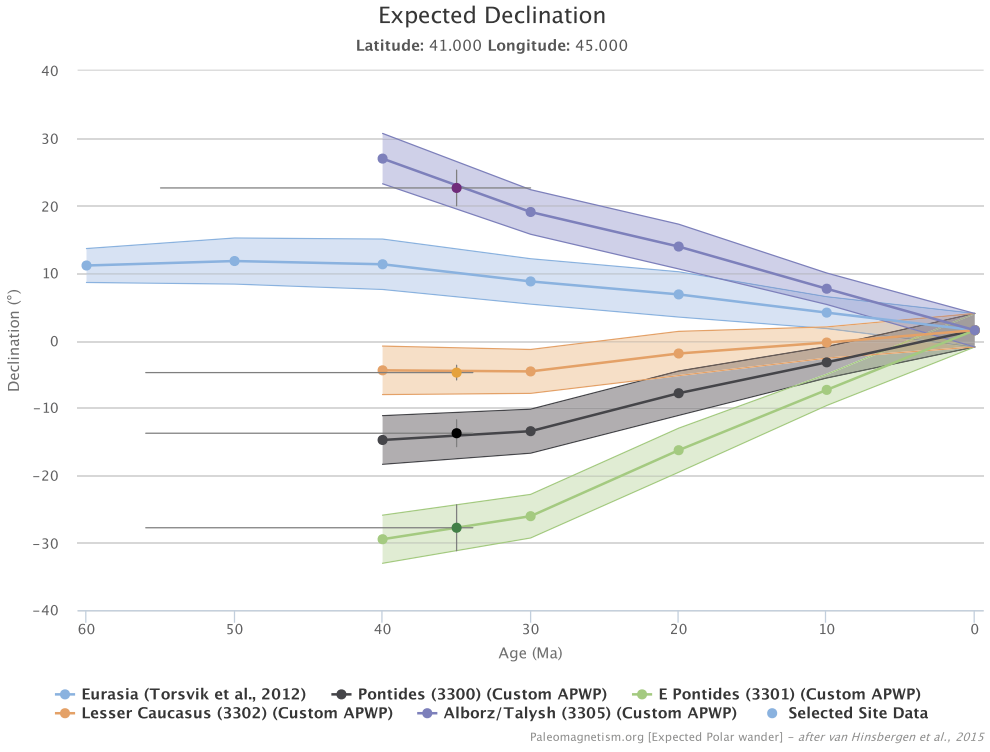

Fig. 7. Apparent polar wander path of Eurasia (Torsvik et al., 2012) compared to the apparent polar wander paths that we calculated for each block (Li et al., 2017) on the basis of the rotation poles of our best fit Gplates reconstruction for a reference location at 41°N, 45°E. The average declination (D; with error ΔD_x) per block is given at 35 Ma; the age error bar spans the entire Eocene.

6. Conclusions

We provide new paleomagnetic data from the Talysh of NW Iran from which we derive a consistent clockwise rotation with a mean declination $D \pm \Delta D_x = 25.9 \pm 6.1°$. We then calculate first order approximations of convergence in the Greater Caucasus region, using kinematic restorations of vertical axis rotations interpreted from paleomagnetic declinations of tectonic blocks in the Eastern Pontides – Lesser Caucasus – Talysh orocline. We estimate convergence taken up in the Greater Caucasus to be a minimum of 120 km in the east, and 200–280 km in the west. Our reconstruction estimates that these domains are separated by a large dextral transform fault zone that accommodated ~160 km of slip since the late Eocene, of which the presently observed Arax fault might have been part. Our results provide independent corroboration of recent estimates of a subducted slab with a length of up to 280 km underneath the Greater Caucasus (Mumladze et al., 2015). Our analysis suggests that ~600 km of post-Eocene Arabia–Europe convergence must have been accommodated in and south of the east Anatolian plateau, and ~780 km within and south of the Iranian plateau. These constraints serve as a boundary condition on future studies that constrain how convergence is partitioned over plateau growth and Neotethyan subduction, and the role of continental collision therein.

Acknowledgements

This work was financially supported by the Netherlands Organization for Scientific Research (NWO) through the VICI grant 865.10.011 of WK and the VIDI grant 864.11.004 of DJJvH, while DJJvH and DG acknowledge ERC Starting Grant number 306810 (SINK). We thank Eric Cowgill, Adam Forte and anonymous reviewers for their comments which improved the manuscript.

Appendix A. Supplementary material

We provide online supplementary information in the form of an appendix. It can be found online at https://doi.org/10.1016/j.epsl.2017.11.025. It contains all GPS data of sites (in decimal degrees, geodetic datum WGS84) as a .kml file, the paleomagnetic data including the *site*.dir and *locality*.pmag files for the web portal Paleomagnetism.org. Our GPlates reconstruction files are supplied as GPlates_Caucasus.gpml and GPlates_rotation.rot. Literature data that went into the reconstruction is supplied in Table A1. Rotation poles that are used for calculating the apparent polar wander paths are supplied in Table A2. Table A3 contains estimated total reconstruction poles at 35 Ma of the four blocks of the Pontides–Lesser Caucasus–Talysh orocline. Rotating the four blocks of the orocline shown in Fig. 6 over these poles obeys the paleomagnetic data of each block (Fig. 7) and were used to estimate total post-35 Ma convergence accommodated within the Caucasus orogen.

References

Adamia, S., Alania, V., Chabukiani, A., Kutelia, Z., Sadradze, N., 2011a. Great Caucasus (Cavcasioni): a long-lived North-Tethyan Back-Arc Basin. Turk. J. Earth Sci. 20, 611–628.

Adamia, S., Zakariadze, G., Chkhotua, T., Sadradze, N., Tsereteli, N., Chabukiani, A., Gventsadze, A., 2011b. Geology of the Caucasus: a review. Turk. J. Earth Sci. 20, 489–544.

Agard, P., Omrani, J., Jolivet, L., Whitechurch, H., Vrielynck, B., Spakman, W., Monié, P., Meyer, B., Wortel, R., 2011. Zagros orogeny: a subduction-dominated process. Geol. Mag. 148, 692–725.

Azizi, H., Moinevaziri, H., 2009. Review of the tectonic setting of Cretaceous to Quaternary volcanism in northwestern Iran. J. Geodyn. 47, 167–179.

Barrier, E., Vriekynck, B., Bergerat, F., Brunet, M.F., Mosar, J., Poisson, A., Sosson, M., 2008. Palaeotectonic maps of the Middle East: tectono-sedimentary-palinspastic maps from Late Norian to Pliocene.

Bazhenov, M.L., Burtman, V.S., 2002. Eocene paleomagnetism of the Caucasus (southwest Georgia): oroclinal bending in the Arabian syntaxis. Tectonophysics 344, 247–259.

Berberian, M., King, G.C.P., 1981. Towards a paleogeography and tectonic evolution of Iran. Can. J. Earth Sci. 18, 210–265.

Biggin, A.J., Van Hinsbergen, D.J.J., Langereis, C.G., Straathof, G.B., Deenen, M.H.L., 2008. Geomagnetic secular variation in the Cretaceous Normal Superchron and in the Jurassic. Phys. Earth Planet. Inter. 169, 3–19.

Chiu, H.-Y., Chung, S.-L., Zarrinkoub, M.H., Mohammadi, S.S., Khatib, M.M., Iizuka, Y., 2013. Zircon U–Pb age constraints from Iran on the magmatic evolution related to Neotethyan subduction and Zagros orogeny. Lithos 162–163, 70–87.

Cifelli, F., Ballato, P., Alimohammadian, H., Sabouri, J., Mattei, M., 2015. Tectonic magnetic lineation and oroclinal bending of the Alborz range: implications on the Iran–Southern Caspian geodynamics. Tectonics 34, 116–132.

Cowgill, E., Forte, A.M., Niemi, N., Avdeev, B., Tye, A., Trexler, C., Javakhishvili, Z., Elashvili, M., Godoladze, T., 2016. Relict basin closure and crustal shortening budgets during continental collision: an example from Caucasus sediment provenance. Tectonics, 2918–2947.

Deenen, M.H.L., Langereis, C.G., van Hinsbergen, D.J.J., Biggin, A.J., 2011. Geomagnetic secular variation and the statistics of palaeomagnetic directions. Geophys. J. Int. 186, 509–520.

Dilek, Y., Altunkaynak, Ş., 2010. Geochemistry of Neogene–Quaternary alkaline volcanism in western Anatolia, Turkey, and implications for the Aegean mantle. Int. Geol. Rev. 52, 631–655.

Doroozi, R., Vaccaro, C., Masoudi, F., Petrini, R., 2016. Cretaceous alkaline volcanism in south Marzanabad, northern central Alborz, Iran: geochemistry and petrogenesis. Geosci. Front. 7, 1–15.

Ershov, A.V., Brunet, M.F., Nikishin, A.M., Bolotov, S.N., Nazarevich, B.P., Korotaev, M.V., 2003. Northern Caucasus basin: thermal history and synthesis of subsidence models. Sediment. Geol. 156, 95–118.

Forte, A.M., Cowgill, E., Whipple, K.X., 2014. Transition from a singly vergent to doubly vergent wedge in a young orogen: the Greater Caucasus. Tectonics 33, 2077–2101.

Ghorbani, M., 2013. The Economic Geology of Iran. Springer.

Gravand, R., Golgir, Z., 2014. Biostratigraphy of the Eocene sediments in Alborz Province, Iran. Adv. Environ. Biol. 8, 1285–1292.

Hisarlı, Z.M., 2011. New paleomagnetic constraints on the late Cretaceous and early Cenozoic tectonic history of the Eastern Pontides. J. Geodyn.

Hollingsworth, J., Jackson, J., Walker, R., Nazari, H., 2008. Extrusion tectonics and subduction in the eastern South Caspian region since 10 Ma. Geology 36, 763–766.

Hüsing, S., Zachariasse, W.-J., van Hinsbergen, D.J.J., Krijgsman, W., Inceöz, M., Harzhauser, M., Mandic, O., Kroh, A., 2009. Oligocene–Miocene basin evolution in SE Anatolia, Turkey: constraints on the closure of the eastern Tethys gateway. In: Collis. Collapse Africa-Arabia–Eurasia Subduction Zo., Geol. Soc. London, Spec. Publ. 311, 107–132.

Jackson, J., Mckenzie, D., 1983. Active tectonics of the Alpine–Himalayan Belt between western Turkey and Pakistan. Geophys. J. R. Astron. Soc. 77, 185–264.

Jackson, J., Priestley, K., Allen, M., Berberian, M., 2002. Active tectonics of the South Caspian Basin. Geophys. J. Int. 148, 214–245.

Koymans, M.R., Langereis, C.G., Pastor-Galán, D., van Hinsbergen, D.J.J., 2016. Paleomagnetism.org: an online multi-platform open source environment for paleomagnetic data analysis. Comput. Geosci. 93, 127–137.

Li, S., Advokaat, E.L., van Hinsbergen, D.J.J., Deng, C., Zhu, R., 2017. Paleomagnetic constraints on the Mesozoic–Cenozoic paleolatitudinal and rotational history of Indochina and South China: review and updated kinematic reconstruction. Earth-Sci. Rev. 171, 58–77.

McFadden, P.L., McElhinny, M.W., 1988. The combined analysis of remagnetization circles and direct observations in palaeomagnetism. Earth Planet. Sci. Lett. 87, 161–172.

McQuarrie, N., van Hinsbergen, D.J.J., 2013. Retrodeforming the Arabia–Eurasia collision zone: age of collision versus magnitude of continental subduction. Geology 41, 315–318.

Meijers, M.J.M., Smith, B., Pastor-Galán, D., Degenaar, R., Sadradze, N., Adamia, S., Sahakyan, L., Avagyan, A., Sosson, M., Rolland, Y., Langereis, C.G., Müller, C., 2015. Progressive orocline formation in the Eastern Pontides – Lesser Caucasus. In: Tectonic Evolution of the Eastern Black Sea and Caucasus, Geol. Soc. (Lond.) Spec. Publ. 428.

Morley, C.K., Kongwung, B., Julapour, A.A.A., Abdolghafourian, M., Hajian, M., Waples, D., Warren, J., Otterdoom, H., Srisuriyon, K., Kazemi, H., 2009. Structural development of a major late Cenozoic basin and transpressional belt in central Iran: the Central Basin in the Qom-Saveh area. Geosphere 5, 325–362.

Mouthereau, F., Lacombe, O., Vergés, J., 2012. Building the Zagros collisional orogen: Timing, strain distribution and the dynamics of Arabia/Eurasia plate convergence. Tectonophysics 532–535, 27–60.

Mumladze, T., Forte, A.M., Cowgill, E.S., Trexler, C.C., Niemi, N.A., Burak Yikilmaz, M., Kellogg, L.H., 2015. Subducted, detached, and torn slabs beneath the Greater Caucasus. GeoResJ 5, 36–46.

Okay, A.I., Özcan, E., Cavazza, W., Okay, Ni., Less, G., 2010. Basement types, Lower Eocene series, Upper Eocene olistostromes and the initiation of the Southern Thrace Basin, NW Turkey. Turk. J. Earth Sci. 19, 1–25.

Rezaeian, M., Carter, A., Hovius, N., Allen, M.B., 2012. Cenozoic exhumation history of the Alborz Mountains, Iran: new constraints from low-temperature chronometry. Tectonics 31.

Rolland, Y., Perincek, D., Kaymakci, N., Sosson, M., Barrier, E., Avagyan, A., 2012. Evidence for ∼80–75 Ma subduction jump during Anatolide–Tauride–Armenian block accretion and ∼48 Ma Arabia–Eurasia collision in Lesser Caucasus–East Anatolia. J. Geodyn. 56–57, 76–85.

Şengör, A.M.C., Özeren, S., Genç, T., Zor, E., Şengör, A.M.C., Özeren, S., Genç, T., Zor, E., 2003. East Anatolian high plateau as a mantle-supported, north–south shortened domal structure. Geophys. Res. Lett. 30, 8045.

Si, J., Van der Voo, R., 2001. Too-low magnetic inclinations in Central Asia: an indication of a long-term Tertiary non-dipole field? Terra Nova 13, 471–478.

Solaymani Azad, S., Dominguez, S., Philip, H., Hessami, K., Forutan, M.R., Shahpasan Zadeh, M., Ritz, J.F., 2011. The Zandjan fault system: morphological and tectonic evidences of a new active fault network in the NW of Iran. Tectonophysics 506, 73–85.

Sosson, M., Rolland, Y., Muller, C., Danelian, T., Melkonyan, R., Kekelia, S., Adamia, S., Babazadeh, V., Kangarli, T., Avagyan, a., Galoyan, G., Mosar, J., 2010. Subductions, obduction and collision in the Lesser Caucasus (Armenia, Azerbaijan, Georgia), new insights. Geol. Soc. (Lond.) Spec. Publ. 340, 329–352.

Stampfli, G.M., Borel, G.D., 2002. A plate tectonic model for the Paleozoic and Mesozoic constrained by dynamic plate boundaries and restored synthetic oceanic isochrons. Earth Planet. Sci. Lett. 196, 17–33.

Torsvik, T.H., Van der Voo, R., Preeden, U., Mac Niocaill, C., Steinberger, B., Doubrovine, P.V., van Hinsbergen, D.J.J., Domeier, M., Gaina, C., Tohver, E., Meert, J.G., McCausland, P.J.A., Cocks, L.R.M., 2012. Phanerozoic polar wander, palaeogeography and dynamics. Earth-Sci. Rev. 114, 325–368.

van der Boon, A., Kuiper, K.F., Villa, G., Renema, W., Meijers, M.J.M., Langereis, C.G., Aliyeva, E., Krijgsman, W., 2015. Onset of Maikop sedimentation and cessation of Eocene arc volcanism in the Talysh Mountains, Azerbaijan. Geol. Soc. (Lond.) Spec. Publ. 428.

Van Hinsbergen, D.J.J., Lippert, P.C., Dupont-Nivet, G., McQuarrie, N., Doubrovine, P.V., Spakman, W., Torsvik, T.H., 2012. Greater India Basin hypothesis and a two-stage Cenozoic collision between, India and Asia. Proc. Natl. Acad. Sci. USA 109, 7659–7664.

Verdel, C., Wernicke, B.P., Hassanzadeh, J., Guest, B., 2011. A Paleogene extensional arc flare-up in Iran. Tectonics 30.

Vincent, S.J., Allen, M.B., Ismail-Zadeh, A.D., Flecker, R., Foland, K.A., Simmons, M.D., 2005. Insights from the Talysh of Azerbaijan into the Paleogene evolution of the South Caspian region. Geol. Soc. Am. Bull. 117, 1513–1533.

Vincent, S.J., Braham, W., Lavrishchev, V.A., Maynard, J.R., Harland, M., 2016. The formation and inversion of the western Greater Caucasus Basin and the uplift of the western Greater Caucasus: implications for the wider Black Sea region. Tectonics 35, 1–15.

Vissers, R.L.M., Van Hinsbergen, D.J.J., Van Der Meer, D.G., Spakman, W., 2016. Cretaceous slab break-off in the Pyrenees: Iberian plate-kinematics in paleomagnetic and mantle reference frames. Gondwana Res. 34, 49–59.

Zanchetta, S., Zanchi, a., Villa, I., Poli, S., Muttoni, G., 2009. The Shanderman eclogites: a Late Carboniferous high-pressure event in the NW Talesh Mountains (NW Iran). Geol. Soc. (Lond.) Spec. Publ. 312, 57–78.

Zanchi, A., Berra, F., Mattei, M., Ghassemi, M.R., Sabouri, J., 2006. Inversion tectonics in central Alborz, Iran. J. Struct. Geol. 28, 2023–2037.